

A Numerical Study on Unsteady Flow Around a Mechanical Pectoral Fin

Hiro Yoshi Suzuki* and Naomi Kato*
 Osaka University, Graduate School of Engineering, Suita, Osaka, Japan

This paper describes the unsteady flow around a mechanical pectoral fin. An unsteady, multiblock, overlapping grid Navier-Stokes equation solver was developed for this problem. The drag-based swimming mode, which consists of rowing, flapping and feathering motions, was selected as the fin motion. An unsteady flow past a fin body model with the same motions was computed and compared with the experiments on the mechanical pectoral fin. The numerical time-averaged and time-varied hydrodynamic forces were in good agreement with the measured data. In addition, the flow phenomenon around the fin was investigated from the flow visualization and computational results.

INTRODUCTION

Several existing underwater vehicles are controlled by thrusters and wings. These vehicles, however, display poor control performance while hovering and turning in a vertical or horizontal plane over an intricate seabed terrain in strong currents. The study of the locomotion of aquatic animals can provide new insights into the maneuverability and stabilization of underwater vehicles.

A number of previous studies on fish fins and their movements has focused on axial undulation and fin oscillation for propulsion (Barrett et al., 1999; Kumph et al., 1999; Triantafyllou et al., 2000; Anderson et al., 2001; Nakashima et al., 2002). Neither axial undulation nor fin oscillation are considered suitable to serve as the main thruster for underwater vehicles. This is because a major drawback of these screw-type thrusters is that they display inadequate measurability, such as in cases where a sudden generation of thrust force occurs due to the hovering of underwater vehicles; this leads to imprecise control of the position and direction of the vehicle and its manipulators. However, such thrusters do not display adequate propulsive performance. In reality, several types of fish use oscillating pectoral fins to maneuver at low swimming speeds (Lindsey, 1978). Based on these considerations, it is possible to overcome the drawbacks of screw-type thrusters by using the pectoral fin movements.

Because of this, underwater vehicles with flapping foils and other fish-like control devices attached to rigid cylinders have been developed (Bandyopadhyay et al., 1997; Hobson et al., 1999; Kato et al., 2002, 2003, 2004; Kato and Liu, 2003).

This research program aims at enhancing and utilizing our understanding of biologically inspired maneuvering systems to expand the operational envelope of marine vehicles. It consists of advanced research on unsteady hydrodynamics and innovative approaches to bioaquatic vehicle control as well as of hardware development for demonstration and performance evaluation.

Our research group has already demonstrated the 3-dimensional swimming performance of an underwater vehicle equipped with 2 pairs of oscillating fins, as well as its control performance in still water, waves and currents (Kato et al., 2003a, 2004). However,

since trial and error are essential to experiments, determining the desired levels of guidance and control laws for the underwater vehicle involves a considerable amount of cost and time. Only then can our research group begin work on the project of developing a numerical motion simulator for underwater vehicles with oscillating fins. Previously, several numerical studies have been conducted on the flow around pectoral fins of fish or oscillating fins (e.g., Kato et al., 2002; Ramamurti et al., 2002; Lui and Kato, 2004); this study differs, however, as it was conducted to determine the first stage in the development of the numerical motion simulator.

This paper presents a portion of the numerical results of the unsteady flow around a mechanical pectoral fin device operated by the drag-based swimming mode, presenting it from the viewpoint of hydrodynamic forces, pressure distribution on the fin, and visualization of the flow field around the fin device.

MECHANICAL PECTORAL FIN

The mechanical pectoral fin device with a cylindrical body shown in Fig. 1a was selected as the fin body model, and an asymmetric fin shown in Fig. 1b was selected as the fin shape for computation. The mechanical pectoral fin was manufactured to experimentally assess the hydrodynamic characteristics of flapping, rowing and feathering motions in the fin system (Kato et al., 2002). The fin is a compact 3-motor-driven mechanical pectoral fin (3MDMPF) device designed to simulate the flapping, rowing and feathering motions of a biological flapping wing or fin, and it possesses high-speed capability and precise movement.

This device is equipped with a force sensor that measures the normal force acting on the rigid fin, and a torque sensor that measures the torque around a fin shaft. Also installed are potentiometers for measuring the angle of the rowing, flapping and feathering motions.

The angle of the rowing motion ranges from -60° to $+70^\circ$; that of the flapping motion, from -60° to $+60^\circ$; and that of the feathering motion, from -180° to $+180^\circ$. The maximum speed of the fin movement is designed to be 3 Hz.

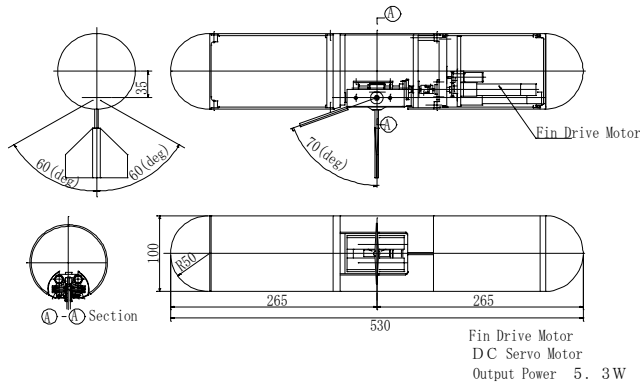
The rowing angle ϕ_R , feathering angle ϕ_{FE} and flapping angle ϕ_{FL} , all of which are defined in Fig. 2, were sinusoidally varied using the following definitions:

$$\begin{aligned}\phi_R &= \phi_{R0} - \phi_{RA} \cdot \cos(\omega_{fin} \cdot t) \\ \phi_{FE} &= \phi_{FE0} - \phi_{FEA} \cdot \cos(\omega_{fin} \cdot t + \Delta\phi_{FE}) \\ \phi_{FL} &= \phi_{FL0} - \phi_{FLA} \cdot \cos(\omega_{fin} \cdot t + \Delta\phi_{FL})\end{aligned}\quad (1)$$

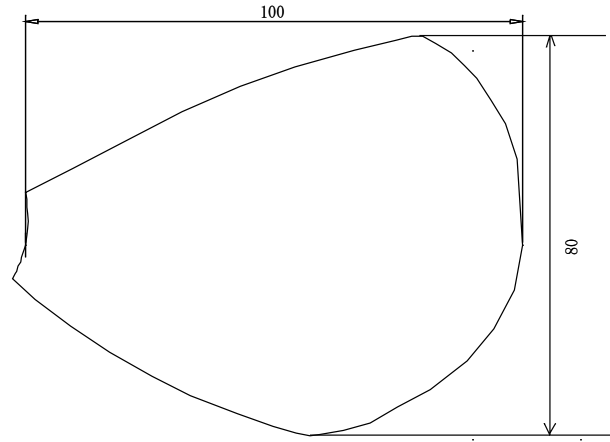
*ISOPE Member.

Received March 30, 2005; revised manuscript received by the editors July 11, 2005. The original version (prior to the final revised manuscript) was presented at the 15th International Offshore and Polar Engineering Conference (ISOPE-2005), Seoul, June 19–24, 2005.

KEY WORDS: Mechanical pectoral fin, Navier-Stokes equation, CFD, chimera grid system, overlapping grid method, unsteady flow, drag-based swimming mode, flow visualization.



(a) Overview of cylindrical body with 3MDMPF device



(b) Fin shape (unit: mm)

Fig. 1 Computational model

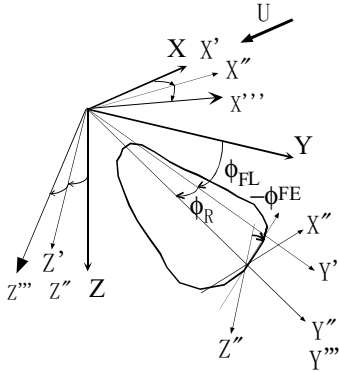


Fig. 2 Coordinate system

where ω_{fin} and t denote the angular velocity of the fin and time, respectively. The swimming mode can be defined by the 8 angular parameters that consist of ϕ_{FL} , ϕ_R and ϕ_{FE} . It is possible to easily change both the drag-based and lift-based swimming modes by varying the parameters appropriately.

NUMERICAL METHOD

Grid Generation

The geometrical properties of a cylindrical body equipped with a mechanical pectoral fin are rather different from those of the mechanical pectoral fin itself. It is difficult to generate a unique

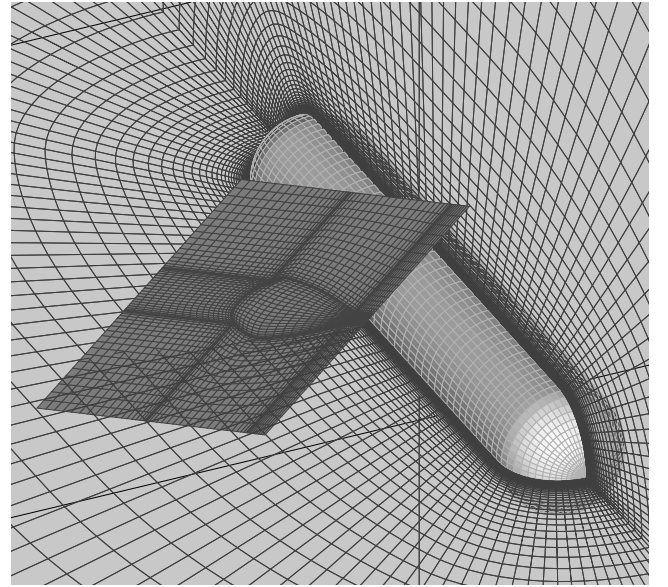


Fig. 3 Grid system

grid system around a cylindrical body and a moving fin in the entire solution domain by using a structure grid system. Thus a chimera grid system was employed to counter this problem.

Computation in the chimera grid system is performed by the overlapping grid method. By employing the chimera grid system, the computational domain can be divided into 2 overlapping grid systems that are easy to generate (Fig. 3).

The main solution domain includes the cylindrical body and outer boundaries, while the subsolution domain located in the main solution domain includes the fin. In each domain, the computational grid is generated independently. O—O type and H—H type boundary-fitted coordinates are generated in the main solution domain and subsolution domain, respectively.

The grid system of the main solution domain is generated around a cylindrical body using $80 \times 61 \times 63$ grid points. The minimum spacing of the grid on the body surface is 0.0001. The outer boundary is set at 1.5 times the length of a cylindrical body. The grid system of the subsolution domain is generated around a fin using $57 \times 49 \times 42$ grid points. The minimum spacing of the grid on the fin surface is 0.001, but the chord length of the fin (C) is selected as the unit length, and the shaft support of the fin at its base is not considered in this computation.

In order to express the fin motion in accordance with the progression of time, the grid points of the subsolution domain were shifted using the following relations:

Feathering:

$$\begin{cases} x_{ijk}^{n1} = x_{pivot} + \cos(\phi_{FE}^n)(x_{ijk}^0 - x_{pivot}) + \sin(\phi_{FE}^n)(z_{ijk}^0 - z_{pivot}) \\ y_{ijk}^{n1} = y_{ijk}^0 \\ z_{ijk}^{n1} = z_{pivot} - \sin(\phi_{FE}^n)(x_{ijk}^0 - x_{pivot}) + \cos(\phi_{FE}^n)(z_{ijk}^0 - z_{pivot}) \end{cases} \quad (2)$$

Flapping:

$$\begin{cases} x_{ijk}^{n2} = x_{ijk}^{n1} \\ y_{ijk}^{n2} = y_{pivot} + \cos(\phi_{FL}^n)(y_{ijk}^{n1} - y_{pivot}) - \sin(\phi_{FL}^n)(z_{ijk}^{n1} - z_{pivot}) \\ z_{ijk}^{n2} = z_{pivot} + \sin(\phi_{FL}^n)(y_{ijk}^{n1} - y_{pivot}) + \cos(\phi_{FL}^n)(z_{ijk}^{n1} - z_{pivot}) \end{cases} \quad (3)$$

Rowing:

$$\begin{cases} x_{ijk}^3 = x_{pivot} + \cos(\phi_R^n)(x_{ijk}^{n2} - x_{pivot}) - \sin(\phi_R^n)(y_{ijk}^{n2} - y_{pivot}) \\ y_{ijk}^3 = y_{pivot} + \sin(\phi_R^n)(x_{ijk}^{n2} - x_{pivot}) + \cos(\phi_R^n)(y_{ijk}^{n2} - y_{pivot}) \\ z_{ijk}^3 = z_{ijk}^{n2} \end{cases} \quad (4)$$

Here, the superscripts 0 and n denote the 0th and n -th time step, and the superscripts 1, 2 and 3 represent the steps of feathering, flapping and rowing motions, respectively. The subscripts i , j and k express the grid point of the subsolution domain, and the subscript *pivot* denotes the pivot point of the origin at the fin.

Governing Equations

The governing equations are the incompressible, unsteady Navier-Stokes equations and the continuity equation:

$$\begin{cases} \frac{\partial u}{\partial t} + u \frac{\partial u}{\partial x} + v \frac{\partial u}{\partial y} + w \frac{\partial u}{\partial z} = -\frac{1}{\rho} \frac{\partial p}{\partial x} + v \left(\frac{\partial^2 u}{\partial x^2} + \frac{\partial^2 u}{\partial y^2} + \frac{\partial^2 u}{\partial z^2} \right) \\ \frac{\partial v}{\partial t} + u \frac{\partial v}{\partial x} + v \frac{\partial v}{\partial y} + w \frac{\partial v}{\partial z} = -\frac{1}{\rho} \frac{\partial p}{\partial y} + v \left(\frac{\partial^2 v}{\partial x^2} + \frac{\partial^2 v}{\partial y^2} + \frac{\partial^2 v}{\partial z^2} \right) \\ \frac{\partial w}{\partial t} + u \frac{\partial w}{\partial x} + v \frac{\partial w}{\partial y} + w \frac{\partial w}{\partial z} = -\frac{1}{\rho} \frac{\partial p}{\partial z} + v \left(\frac{\partial^2 w}{\partial x^2} + \frac{\partial^2 w}{\partial y^2} + \frac{\partial^2 w}{\partial z^2} \right) \end{cases} \quad (5)$$

$$\frac{\partial u}{\partial x} + \frac{\partial v}{\partial y} + \frac{\partial w}{\partial z} = 0 \quad (6)$$

where x , y and z are the axes of the orthogonal coordinate system defined in Fig. 2, while u , v and w are the fluid velocity vectors in each direction, p is the pressure, and ρ the fluid density. Turbulence quantities were not considered in the governing equations because the laminar flow was assumed for this computation. All the fluid variables were made dimensionless with respect to the uniform inflow U_0 , the chord length of the fin C , and the fluid density ρ . The dimensionless parameter of the Reynolds number (Rn) is defined as:

$$Rn = \frac{U_0 C}{\nu} \quad (7)$$

where ν is kinetic viscosity.

Boundary Conditions

The boundary of the main solution domain comprises the outer boundary and body surface, and that of the subsolution domain also comprises the outer boundary and fin surface boundary. The outer boundary of the main solution domain is divided into the inflow boundary and the outflow boundary.

The inflow velocity vector is fixed to have a uniform flow ($u = 1$, $v = 0$, $w = 0$), and the pressure is set at zero at the inflow boundary of the main solution domain. The outflow velocity components and pressure are assumed by zero extrapolation ($\partial(u, v, w, p)/\partial n = 0$) at the outflow boundary of the main solution domain. On the body surface, the non-slip condition and zero-gradient condition are imposed for the velocity components and the pressure, respectively.

The velocity components and pressure are set by interpolating the flow variables of the main solution domain on the outer boundary of the subsolution domain, and the boundary condition of the fin surface is set as follows:

$$\begin{aligned} (u, v, w) &= (u_{fin}, v_{fin}, w_{fin}) \\ \frac{\partial p}{\partial n} &= \mathbf{a}_{fin} \cdot \mathbf{n} \end{aligned} \quad (8)$$

where u_{fin} , v_{fin} and w_{fin} denote the velocity of the fin itself in the x , y and z axis, respectively. In addition, \mathbf{a}_{fin} denotes the acceleration of the fin, and \mathbf{n} denotes the normal vector on the fin surface.

It should be noted that $(u_{fin}, v_{fin}, w_{fin})$ and \mathbf{a}_{fin} are determined by the fin motion, and their values are calculated by the finite difference method using the grid points of the subsolution domain.

Navier-Stokes Equation Solver

An unsteady, multiblock, overlapping grid Navier-Stokes equation solver (NS solver) was developed based primarily on a solver established by Stern et al. (1996). The outline of the NS solver is presented below.

The finite analytic method and Euler implicit scheme were employed for spatial discretization and time integration of the governing equations, respectively, and the PISO-type one-step procedure was employed for velocity-pressure coupling.

The dual time stepping (pseudo time iteration) method, which expediently divided the time derivative of the governing equations into 2 parts, was employed for time integration in order to obtain a time-accurate solution. The moving grid method was also implemented in the governing equations of the subsolution domain. The simultaneous linear equations of fluid velocity u , v and w , and pressure p were solved by the SSOR method.

Solution Procedure

In the overlapping grid method, the flow computations were performed iteratively between 2 grid systems, and the flow information was exchanged between the grids by interpolating the flow variables at each pseudo time step. Consequently, the overall solution procedure for this NS solver is as follows:

1. Shift the numerical grid of the subsolution domain in accordance with the defined rowing, flapping and feathering angles at $t = n\Delta t$.
2. Determine the grid points within the overlapping region of the 2 grid systems.
3. Calculate the parameters for the interpolation from the positional relation of the 2 grid systems and store them.
4. Set the boundary condition of the subsolution domain by interpolating the flow variables of the main solution domain.
5. Solve the flow variables in the subsolution domain.
6. Set the inner boundary condition of the main solution domain by interpolating flow variables of the subsolution domain.
7. Solve the flow variables of the main solution domain.
8. Proceed to step 9 if steady solutions are computed in the pseudo time step; if not, return to step 4.
9. Return to step 1, the time step is increased.

Computational Condition

The computational condition of the pectoral fin is based on the input data of the experiments that were previously carried out by using a cylindrical body with a 3MDMPF in the circulating water channel. The movements of the mechanical pectoral fin are expressed by 3 angles (Euler angles) represented in Eq. 1, and these Euler angles are defined by 8 parameters. In this study, the values of the parameters ϕ_{R0} , ϕ_{RA} , ϕ_{FE0} , ϕ_{FEA} , ϕ_{FLO} , ϕ_{FLA} and $\Delta\phi_{FE}$ were taken as 30°, 30°, 30°, 30°, 0°, 20° and 90°, respectively. The phase difference between the rowing and flapping motions $\Delta\phi_{FL}$ was set at different values of 0°, 30°, 60° and 90° for the computation.

Fig. 4 shows a representative data set of the instantaneous angles in one cycle. The fin motion was considered to become

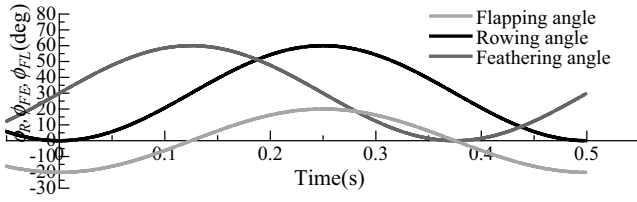


Fig. 4 Example of time variation for flapping, rowing and feathering angles ($\Delta\phi_{FL} = 0^\circ$)

the power stroke in the time interval from $t = 0$ to 0.25 s, and the recovery stroke in the time interval from $t = 0.25$ to 0.5 s because the flapping angle does not coincide with the rowing angle.

In these experiments, the inflow velocity U_0 and frequency of the mechanical pectoral fin motion f were set at 0.251 m/s and 2 Hz (the period $T = 0.5$ s), respectively. Based on these conditions, the reduced frequency $K = 2\pi f C / U_0$ and the Reynolds number were set at 4 and 2.001×10^4 , respectively. In addition, the computation's time step (Δt) was set at 0.00390625 (400 steps in a period) in the dimensionless time.

It should be noted that, although the computation was carried out in 2 cycles of the fin motion, the computational results were evaluated only in the 2nd period, because the results of the 1st period included a nonperiodic feature due to the impulsive start of the fin motion.

RESULTS AND DISCUSSION

Hydrodynamic Forces

Fig. 5 shows the time variations of the hydrodynamic coefficients C_x , C_y and C_z in various phase differences between the rowing and flapping motions $\Delta\phi_{FL}$. In this figure, the solid blue lines represent the computational results, and the black dots represent the measured data. C_x , C_y and C_z are defined as follows:

$$C_x \equiv \frac{F_x}{1/2\rho S U_0^2}, \quad C_y \equiv \frac{F_y}{1/2\rho S U_0^2}, \quad C_z \equiv \frac{F_z}{1/2\rho S U_0^2} \quad (9)$$

However, F_x , F_y and F_z represent the hydrodynamic forces of the x , y and z directions, respectively, and S represents the pectoral fin's surface area. The computational hydrodynamic forces (F_x ,

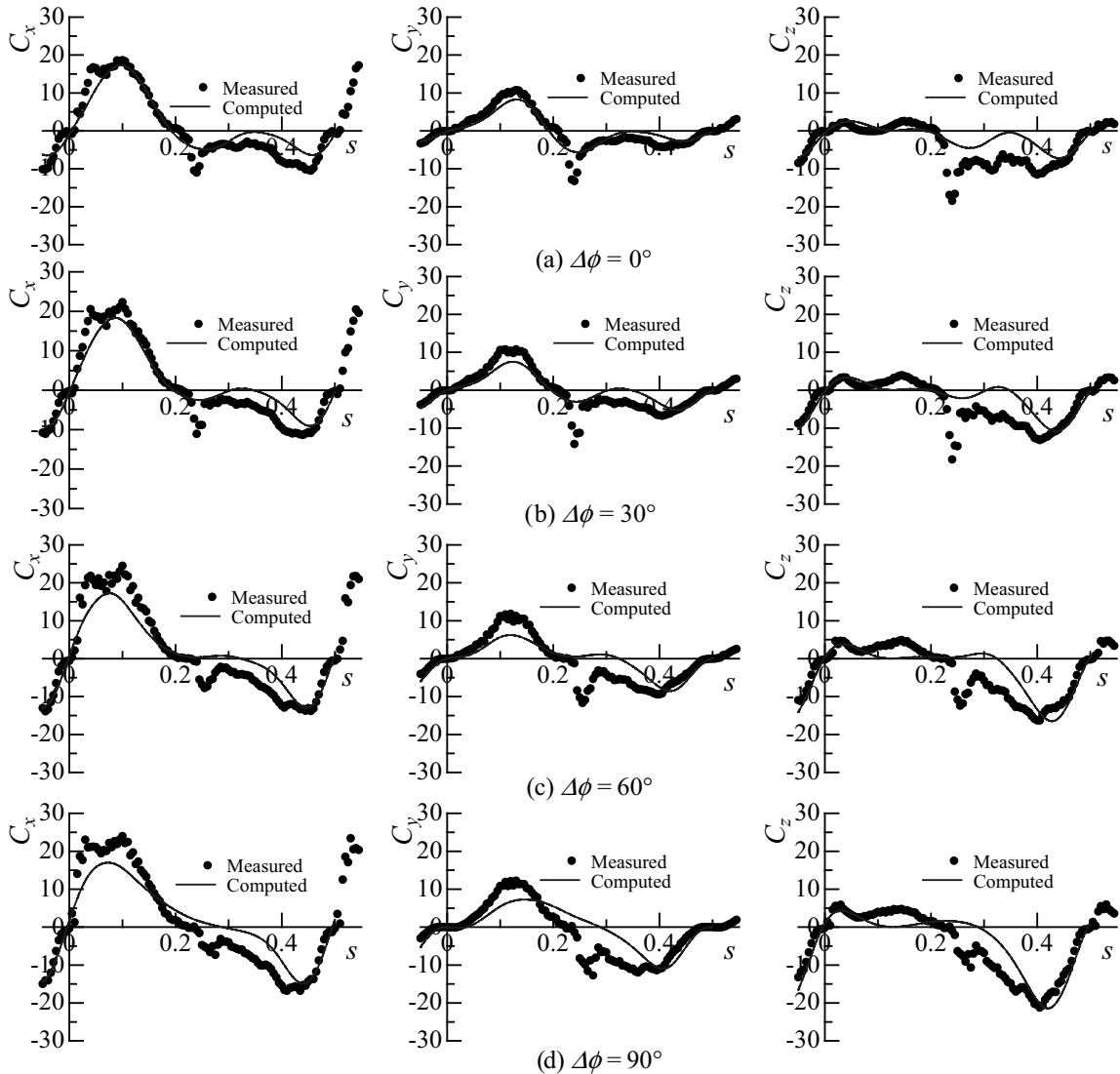


Fig. 5 Time variations of hydrodynamic force coefficients in a cycle

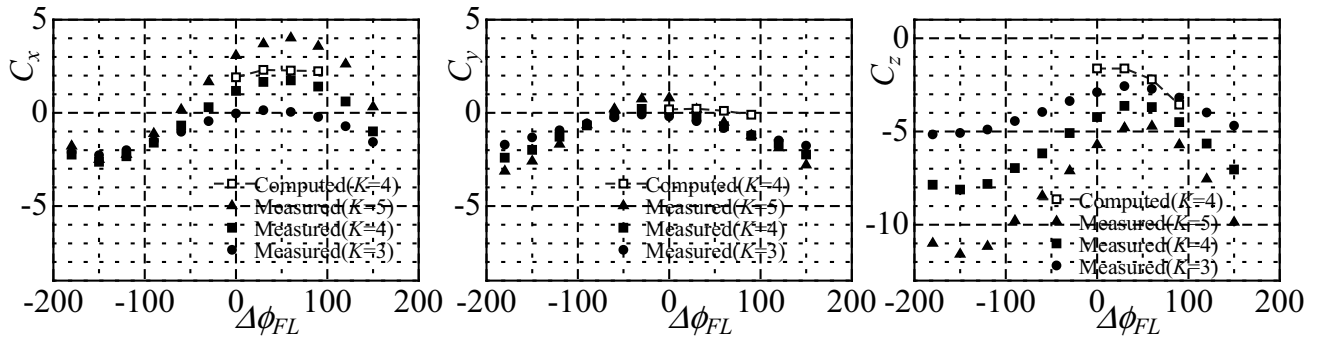


Fig. 6 Comparison of time-averaged hydrodynamic force coefficients between measured and computation results

F_y and F_z) were calculated by the integration of the pressure and velocity gradient on the fin surface.

Overall, the computational hydrodynamic force coefficients show good agreement with the measured data in the instantaneous phase variation and in the magnitude of the 3 force components in all phase differences between the rowing and flapping motions $\Delta\phi_{FL}$.

In particular, as is evident from both the computed and measured data, thrust is generated during the interval $t = 0$ to 0.25 s (power stroke), and drag appears during the interval $t = 0.25$ to 0.5 s (recovery stroke) for all phase differences $\Delta\phi_{FL}$ related to the C_x distribution. The bottom value within the recovery stroke decreases with an increase in the phase difference $\Delta\phi_{FL}$. The same tendency is observed in C_y and C_z . When the phase difference $\Delta\phi_{FL}$ is 0° , the computed value C_x is in good agreement with the measured C_x in the power stroke. In contrast, when the phase difference $\Delta\phi_{FL}$ becomes 90° , both the computed and measured C_x show good agreement. It appears that disregarding the fin shaft could be one of the reasons for the difference that can be observed between the computed and measured coefficients in the plots.

Fig. 6 plots the computed and measured time-averaged (in the 2nd period) hydrodynamic coefficients. The computed time-averaged hydrodynamic coefficient C_x showed good agreement with the measured data, and C_y and C_z showed a similar tendency with the measured data. It is possible that the omission of

the fin shaft during the computation is one of the reasons for the slight difference between the computed and measured hydrodynamic coefficients.

It should be noted that the hydrodynamic force of the mechanical pectoral fin referred to in this paper was measured as a part of the author’s former research (Kato et al., 2002; Kato and Liu, 2003).

Pressure Distribution on Fin Surface

Fig. 7 shows the pressure distribution on the fin surface. This presents a case in which the phase difference between the rowing and flapping motions $\Delta\phi_{FL}$ is 0° . The upper column shows the fin’s face side, and the lower column its backside. Here, the negative pressure on the fin’s face side and positive pressure on its backside show the generation of the thrust, while the negative pressure on the backside and positive pressure on the face side show the generation of the drag.

At $t = 0$ s, no characteristic pressure distribution is observed on either side. At $t = 0.1$ s ($1/5T$), in the power stroke, a negative pressure is generated near the tip on the face side, and a positive pressure is widely distributed on the backside of the fin. This implies that a tip vortex is generated near the edge of the fin on the face side, and the fin pushes considerable fluid into the downstream region on the fin’s backside. In addition, these demonstrate the generation of a large thrust at $t = 0.1$. The small

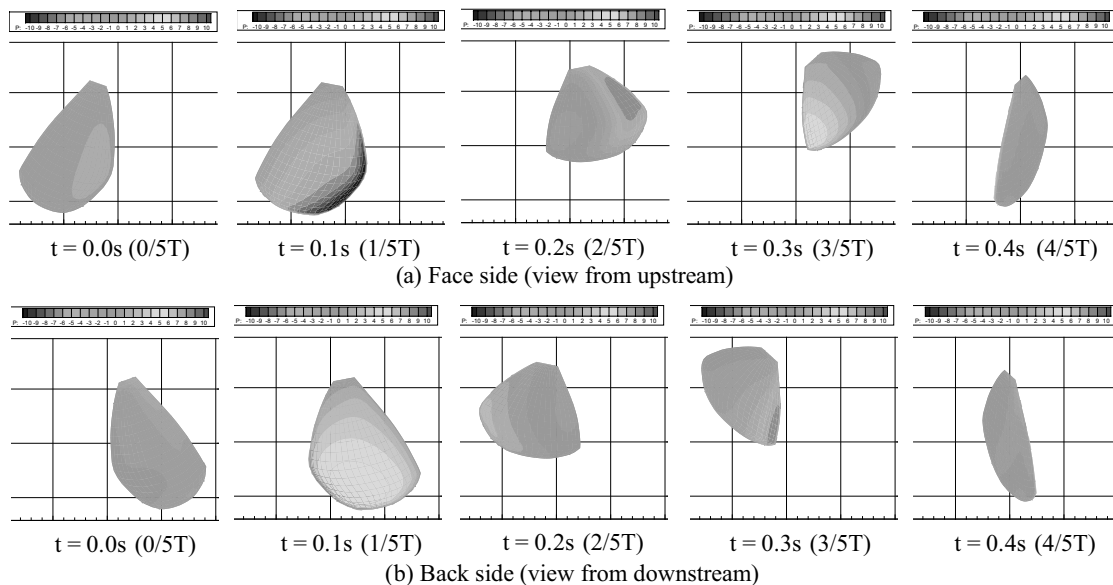


Fig. 7 Pressure distribution on fin surface ($\Delta\phi_{FL} = 0^\circ$)

negative pressure distribution on the fin's face side moves to the fin's root, and a positive pressure distribution is observed near the fin's tip at $t = 0.2$ s ($2/5T$). At this point, the power stroke has almost ended. At $t = 0.3$ s ($3/5T$), immediately after the recovery stroke has begun, one observes a small positive pressure distribution on the fin's face side and a negative pressure distribution on its backside. This shows the generation of the drag. Finally, the pressure is almost zero on both sides of the fin at $t = 0.4$ s ($4/5T$). A relationship—similar to the vortices' generation noted above—is considered to exist between the time variations of the pressure distribution on the fin and the vortices.

Flow Visualization

Flow visualization to confirm the relationship between the vortex and the pressure distribution on the fin surface was carried out in the circulating water channel at Osaka University. The con-

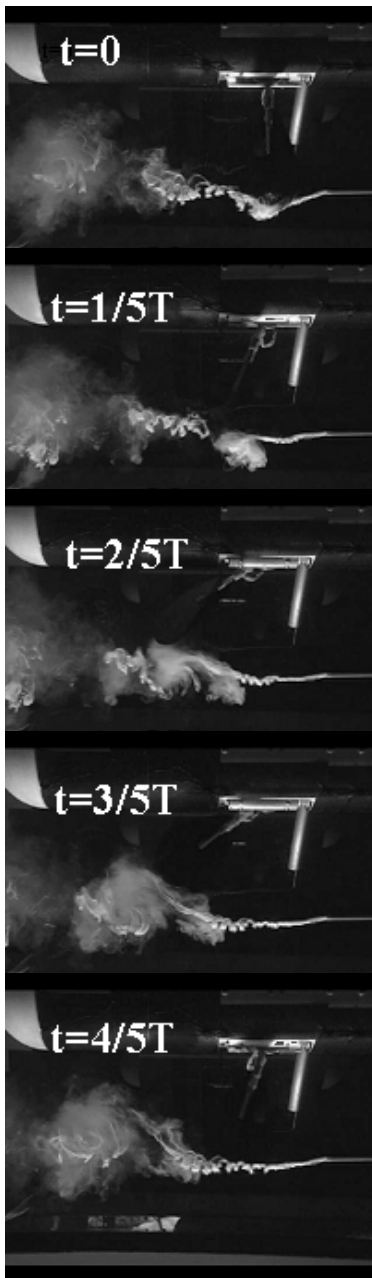


Fig. 8 Flow visualization around mechanical pectoral fin

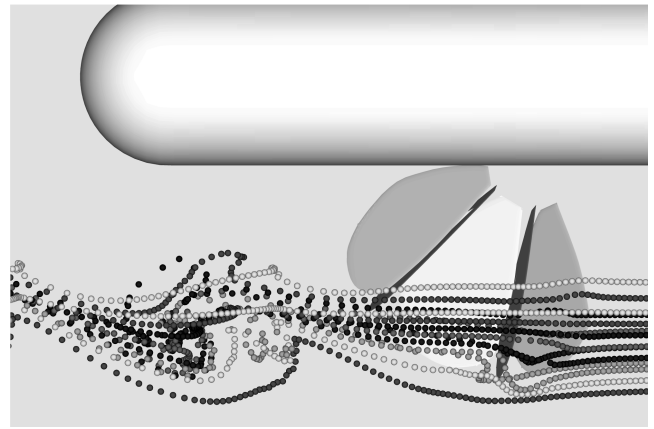


Fig. 9 Computed streak lines around mechanical pectoral fin

densified milk method was applied to the flow visualization technique. A digital video camera was used for image recording. Fig. 8 shows images of the flow visualization. In these images, the inflow is entering from the right-hand side. However, the inflow velocity corresponded to 0.06 m/s, and the angular velocity of the fin was set at 0.5 Hz ($T = 2.0$ s) due to the rapid diffusion of the milk, and the reduced frequency K became 4. Further, the phase difference between the rowing and flapping motions $\Delta\phi_{FL}$ was set at 0° .

At $t = 0$, a clockwise vortex is observed near the tip of the fin. An anti-clockwise vortex is generated near the fin's tip in the upstream region at $t = 1/5T$. Then, it is supposed that the negative pressure is generated near the tip on the face side of the fin. Starting from $t = 2/5T$ up to $4/5T$, the anti-clockwise vortex moves to the downstream region and diffuses widely. These images show that the oscillating fin generates a large-scale vortex emission in the flow field.

Fig. 9 plots the streak lines of the computational result. The vortex phenomenon shown in the flow visualization is also evident from the computational result.

From these results, the negative pressure distribution near the tip on the face side of the fin surface is held to be generated by this tip vortex.

CONCLUSIONS

An unsteady, multiblock, overlapping grid Navier-Stokes equation solver was developed and applied to solve the unsteady flow around a mechanical pectoral fin. The computed time-averaged and time-varied hydrodynamic force coefficients showed good agreement with the experimental results. Further, the variations in hydrodynamic force coefficients due to the phase differences could be resolved. It was confirmed from the flow visualization and computational results that the pressure distribution on the fin is closely related to the vortex phenomena in the flow field.

On the basis of these results, a motion simulator for underwater vehicles with flapping foils will be developed in the near future.

ACKNOWLEDGEMENTS

The authors wish to thank Prof. Y. Toda and Mr. Y. Sanada, Osaka University, for their valuable discussion and their help in conducting the flow visualization in the University's circulating water channel.

REFERENCES

- Anderson, JM, and Kerrebrock, PA (1999). “The Vorticity Control of an Unmanned Undersea Vehicle (VCUUV) Performance Results,” *Proc 11th Int Symp Unmanned, Untethered Submersible Tech*, pp 360–369.
- Bandyopadhyay, PR, Castano, JM, Rice, JQ, Philips, RB, Nederman, WH, and Macy, WK (1997). “Low-speed Maneuvering Hydrodynamics of Fish and Small Underwater Vehicles,” *J Fluids Eng, Trans ASME*, Vol 119, pp 136–144.
- Barrett, DS, Triantafyllou, MS, Yue, DKP, Grosenbaugh, MA, and Wolfgang, MJ (1999). “Drag Reduction in Fish-like Locomotion,” *J Fluid Mech*, Vol 392, pp 183–212.
- Hobson, B, Murray, M, and Pell, C (1999). “Pilotfish: Maximizing Agility in an Unmanned Underwater Vehicle,” *Proc 11th Int Symp Unmanned, Untethered Submersible Tech*, pp 1–51.
- Kato, N, Liu, H, and Morikawa, H (2002). “Biology-inspired Precision Maneuvering of Underwater Vehicles,” *Proc 12th Int Offshore and Polar Eng Conf*, Kitakyushu, Japan, ISOPE, Vol 2, pp 269–276.
- Kato, N, Liu, H, and Morikawa, H (2003). “Biology-inspired Precision Maneuvering of Underwater Vehicles (Part 2),” *Proc 13th Int Offshore and Polar Eng Conf*, Honolulu, ISOPE, Vol 2, pp 178–185.
- Kato, N, and Liu, H (2003). “Optimization of Motion of a Mechanical Pectoral Fin,” *JSME Int J*, Japan, Vol 46, No 4, pp 1356–1362.
- Kato, N, Liu, H, and Morikawa, H (2004). “Biology-inspired Precision Maneuvering of Underwater Vehicles (Part 3),” *Int J Offshore and Polar Eng*, ISOPE, Vol 15, No 2, pp 81–87.
- Kumph, JM, Triantafyllou, MS, Nugent, D, and Santos, MD (1999). “Fast-starting and Maneuvering Vehicles: Robopike and Robomuskie,” *Proc 11th Int Symp Unmanned, Untethered Submersible Tech*, pp 439–445.
- Lindsey, CC (1978). “Form, Function and Locomotory Habits in Fish,” *Fish Physiology VII Locomotion*, WS Hoar and DJ Randall, eds, Academic Press, pp 239–313.
- Lui, H, and Kato, N (2004). “Computation of Unsteady Flow Past a Biomimetic Fin,” *J Bionics Eng*, Vol 1, No 2, pp 108–120.
- Nakashima, M, and Ono, K (2002). “Development of a Two-joint Dolphin Vehicle,” *Neurotechnology for Biomimetic Vehicles*, J Ayers, JJ Davis and A Rudolph, eds, MIT Press, pp 309–324.
- Ramamurti, R, Sandberg, WC, Löhner, R, and Walker, JA (2002). “Fluid Dynamics of Flapping Aquatic Flight in the Bird Wrasse: Three-Dimensional Unsteady Computations with Fin Deformation,” *J Experim Biol*, Vol 205, pp 2997–3008.
- Stern, F, Paterson, EG, and Tahara, Y (1996). “CFDSHIP-IOWA: Computational Fluid Dynamics Method Surface-Ship Boundary Layers, Wakes, and Wave Fields,” *IJHR Rept*, No 381.
- Triantafyllou, MS, Triantafyllou, GS, and Yue, DKP (2000). “Hydrodynamics of Fishlike Swimming,” *Ann Rev of Fluid Mech*, Vol 32, pp 33–53.